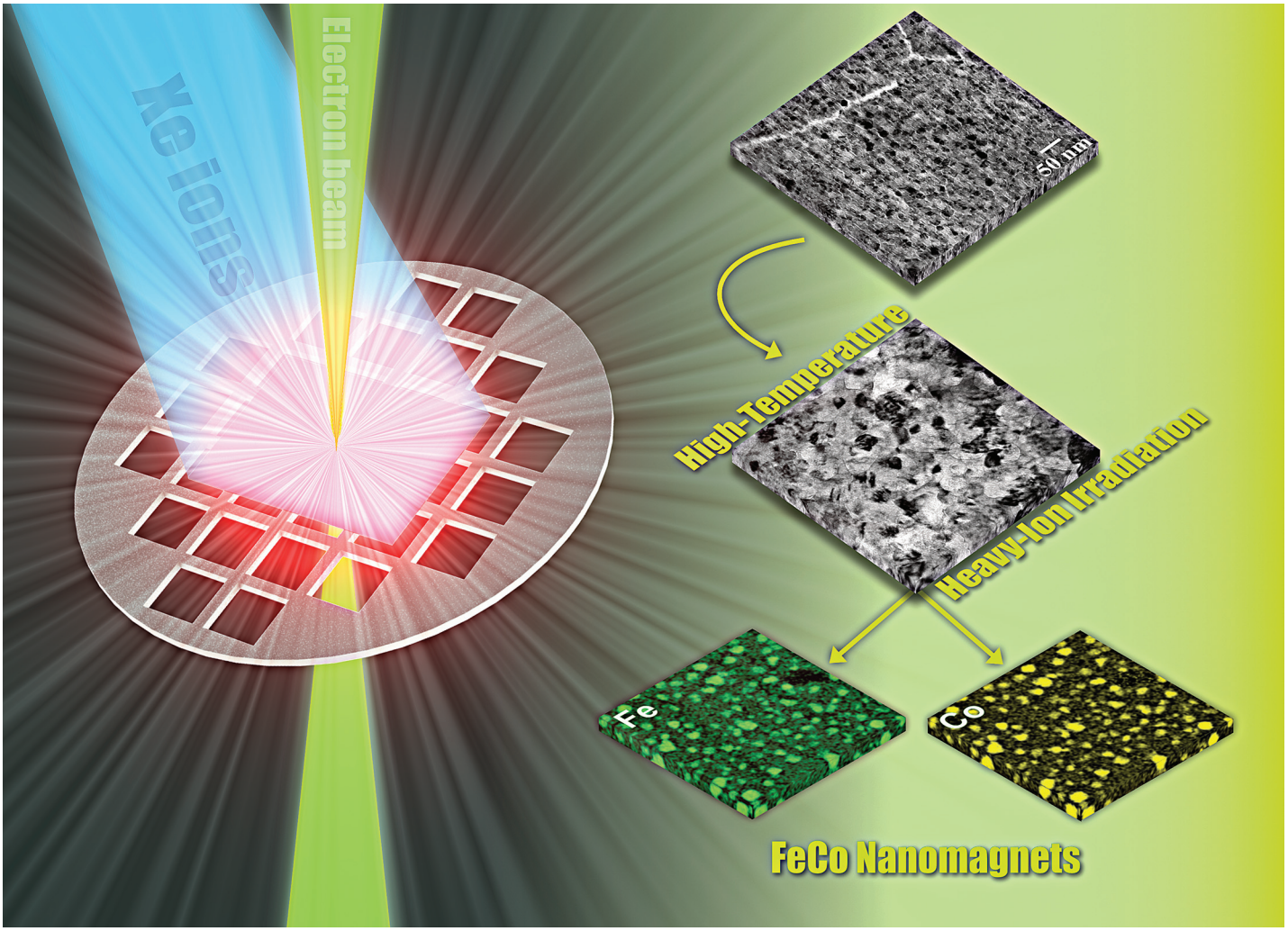

Showcasing research from Los Alamos and Oak Ridge National Laboratories (USA) in partnership with MIAMI Facilities (UK), University of Tennessee (USA), University of São Paulo (Brazil) and Montanuniversität Leoben (Austria).

Irradiation stability and induced ferromagnetism in a nanocrystalline CoCrCuFeNi highly-concentrated alloy

A novel nanocrystalline high-entropy alloy was subjected to extreme irradiation and temperature conditions using *in situ* TEM. Remarkably, the formation of FeCo nanomagnets monodomains was revealed at the nanoscale.

As featured in:

See Matheus A. Tunes *et al.*, *Nanoscale*, 2021, **13**, 20437.

ROYAL SOCIETY OF CHEMISTRY

rsc.li/nanoscale

Registered charity number: 207890

Nanoscale

PAPER

View Article Online
View Journal | View Issue

Cite this: *Nanoscale*, 2021, **13**, 20437

Irradiation stability and induced ferromagnetism in a nanocrystalline CoCrCuFeNi highly-concentrated alloy†

Matheus A. Tunes, *[a] Graeme Greaves,[b] Philip D. Rack,[c,d] Walker L. Boldman,[d] Cláudio G. Schön,[e] Stefan Pogatscher,[f] Stuart A. Maloy,[a] Yanwen Zhang[d,g] and Osman El-Atwani[a]

In the field of radiation damage of crystalline solids, new highly-concentrated alloys (HCAs) are now considered to be suitable candidate materials for next generation fission/fusion reactors due to recently recorded outstanding radiation tolerance. Despite the preliminarily reported extraordinary properties, the mechanisms of degradation, phase instabilities and decomposition of HCAs are still largely unexplored fields of research. Herein, we investigate the response of a nanocrystalline CoCrCuFeNi HCA to thermal annealing and heavy ion irradiation in the temperature range from 293 to 773 K with the objective to analyze the stability of the nanocrystalline HCA in extreme conditions. The results led to the identification of two regimes of response to irradiation: (i) in which the alloy was observed to be tolerant under extreme irradiation conditions and (ii) in which the alloy is subject to matrix phase instabilities. The formation of FeCo monodomain nanoparticles under these conditions is also reported and a differential phase contrast study in the analytical electron-microscope is carried out to qualitatively probe its magnetic properties.

Received 28th July 2021,
Accepted 29th September 2021

DOI: 10.1039/d1nr04915a

rsc.li/nanoscale

1. Introduction

Highly-concentrated alloys (HCAs) (a.k.a. "high-entropy alloys" or HEAs) comprise an entire class of new metallic alloys that are produced with equimolar proportions between multiple alloying constituents (4–5 or more).[1–3] The HCA concept is in contrast to the conventional terminal solid solution principle which is nowadays responsible for the commercialization of the so-called diluted solid solution alloys based on a single element (*e.g.* Fe-based alloys or steels). HCAs may represent an ongoing revolution within metallurgy as they have often been reported to have superior mechanical and corrosion resistances[4–6] than diluted alloys, although the underlying physical mechanisms and the intrinsic alloy core-effects behind these extraordinary properties are not yet well understood.[7–13]

A major goal in metallurgy is the design of new metallic alloys that combine superior strength and ductility with enhanced physico–chemical properties. After synthesis and specific processing, polycrystalline metallic alloys have grain sizes within the microscale which will then define the set of macroscopic properties associated with their final application. Historically, the properties of metallic alloys can be tailored by controlling their final microstructure parameters. In this sense, the emergence of nanometallurgy embraces new strategies aimed at reducing the grain-size of metallic alloys towards the nanoscale, presumably resulting in an enhancement of a wide variety of physical and mechanical properties. This has yielded unprecedented gains for the design of future metallic alloys.[14,15]

It is well known that nanograins (<100 nm) are able to hinder the glide of dislocations during deformation processes, directly leading to higher strength when compared with micrometre-sized grains in conventional alloys.[16–22] A particular field of technology where the potential application of nanocrystalline alloys has been under active consideration is in the selection of appropriate structural materials for the next generation of fission and fusion reactors, by mitigating the generation and by controlling the diffusion of crystal defects at the nanoscale.[23–31] An increased density of grain boundaries acting as active sinks for crystalline defects produced from energetic collisions has

[a]*Materials Science and Technology Division, Los Alamos National Laboratory, USA. E-mail: tunes@lanl.gov*
[b]*School of Computing and Engineering, University of Huddersfield, UK*
[c]*Joint Staff Center of Nanophase Materials Sciences, Oak Ridge National Laboratory, USA*
[d]*Materials Science and Engineering Department, University of Tennessee, USA. E-mail: yzhang1@ornl.gov*
[e]*Department of Metallurgical and Materials Engineering, Escola Politécnica, Universidade de São Paulo, Brazil*
[f]*Chair of Nonferrous Metallurgy, Montanuniversitaet Leoben, Austria*
[g]*Materials Science and Technology Division, Oak Ridge National Laboratory, USA*
†Electronic supplementary information (ESI) available. See DOI: 10.1039/d1nr04915a

been recently reported to be the main reason of enhanced radiation resistance of many metals and alloys when compared with their coarse-grained alloy counterparts.[26–28]

The major challenge for application of nanocrystalline materials in extreme environments remains to prevent the manifestation of degradation mechanisms resulting in microstructural instabilities such as grain growth[24,26,30–36] and phase transformations.[37–42] In order to do so, the nanocrystalline idea has been recently combined with the HCA concept.[4–6,43] Recent research indicated these emergent equiatomic metallic alloys can exhibit improved levels of radiation resistance when compared with conventional nuclear materials such as Zr- and Fe-based alloys.[19,26,27,35,41,44–47] With respect to the application of HCAs as nuclear materials, some challenges are still pending when it comes to their radiation response: phase stability at high temperature irradiation[7,48,49] and, in addition, the occurrence of radiation-induced precipitation and segregation (RIP/RIS).[28]

Degradation, phase transformations, segregation and precipitation studies on HCAs are still limited, but some recent works have addressed this problem. Santodonato *et al.*[50] investigated the influence of small Al additions in the high-temperature response of the CoCrCuFeNi HCA. The synthesized alloy had large grains in the mesoscale ("hundreds of microns" according to the authors[50]). They reported the occurrence of a distinct spinodal decomposition of the alloy matrix phase into several classes of CoCrFe-rich BCC (B2) nanoprecipitates and Cu-partition, although concluding that the characteristic disorder of HCA system is preserved given the distribution of multiple elements in both detected secondary phases and remaining matrix. Similar results were obtained by Xu *et al.*[51] working with the same alloy system with grain sizes still in the mesoscale ranging from 100 nm to 1.8 μm. Similarly to Santodonato *et al.*,[50] Xu *et al.* also reported on Cu-partition from the alloy matrix and also the formation of ordered FeCoCr(Ni)-rich domains upon annealing.

These works serve as motivation for further studies to investigate whether nanocrystallinity can help HCAs to prevent degradation and phase transformations either under high-temperature annealing or energetic particle irradiation.

A fundamental study on the metallurgical phase stability under annealing and heavy-ion irradiation of a nanocrystalline HCA was carried out in this work. The main objectives of this present work are to investigate the response of the nanocrystalline alloy when subjected to the extreme conditions. Although nanocrystalline alloys are widely studied today, the mechanisms by which they degrade upon irradiation and also annealing – *e.g.* grain growth and phase transformations – are largely unknown.[36] For this, an equiatomic CoCrCuFeNi alloy – which is a modified version of the classical Cantor's alloy[1,2] (CoCrMnFeNi) – was subjected to thermal annealing and heavy ion irradiation *in situ* within a TEM over a wide range of temperatures. The alloy was pre- and post-irradiation characterised using energy dispersive X-ray spectroscopy (EDX) and differential phase contrast (DPC) within a scanning transmission electron microscope (STEM). In addition, a detailed study on grain growth during both irradiation and annealing was carried out using selected area diffraction (SAED) and bright-field transmission electron microscopy (BFTEM). The results shed light that in the regime where the diffusion of vacancies is limited (298–573 K), grain growth is prevented due to the solute drag effect along the interfaces. In the regime where vacancies are mobile ($T > 573$ K), the alloy transforms to another state with the observation of a magnetic nanophase composed of Fe and Co. It is demonstrated that by simply replacing Mn by Cu in a well-known HCA system, the thermodynamic stability – presumed to be high for HCAs – can be disrupted, but gives rise to the formation of a potential functional material composed of monodomains with high magnetization saturation at the nanoscale.

2. Experimental procedures

2.1. Synthesis of nanocrystalline CoCrCuFeNi HCA

The nanocrystalline HCA was synthesised using the magnetron sputtering technique.[52] An equiatomic composition target of diameter 50 mm was fabricated from 99.99% (wt%) pure metals of Ni, Fe, Co, Cr and Cu. The alloy was deposited directly onto a pure NaCl crystal substrate in order to facilitate the TEM specimen preparation. Prior to deposition, a DC supply was used and the magnetron sputtering system was pumped to $\approx 1 \times 10^{-7}$ Torr. For the deposition, an Ar flow rate of 25 sccm was set to equilibrate the system at 5 mTorr and the power at the target was set to a DC power of 200 W. The target was pre-sputtered for 5 min with the shutter closed. Scanning electron microscopy was used to determine the deposition rate, herein estimated to be 7 nm min^{-1}. Under these conditions, the final thickness of the deposited film was measured to be 70 ± 2 nm. The films synthesized in this work were deposited at room temperature. Further details on the deposition method can be found elsewhere.[52]

2.2. Electron-transparent specimen preparation

The electron-transparent samples of the sputter-deposited nanocrystalline HCA were prepared by dissolving the NaCl substrate in a solution containing deionised water and ethanol. The floating nanocrystalline CoCrCuFeNi HCA samples were attached to Mo mesh TEM grids which were then dried in a furnace at 333 K over 15 min.

2.3. Heavy ion irradiation *in situ* within a TEM

Medium-energy heavy ion irradiations *in situ* within a Hitachi H-9500 TEM (operating at 300 kV) were carried out using the MIAMI-2 system at University of Huddersfield.[53] The Xe^+ ion beam energy was set to 134 keV and, under these conditions, the implantation depth and the damage profiles are nearly uniform across the TEM specimens whose thicknesses are around 70 nm as shown in the supplementary Fig. 1. The samples were irradiated with a flux of 5.5×10^{12} ions per cm^2 per s at the temperatures of 273 (or RT), 573 and 773 K using a Gatan double-tilt heating holder.

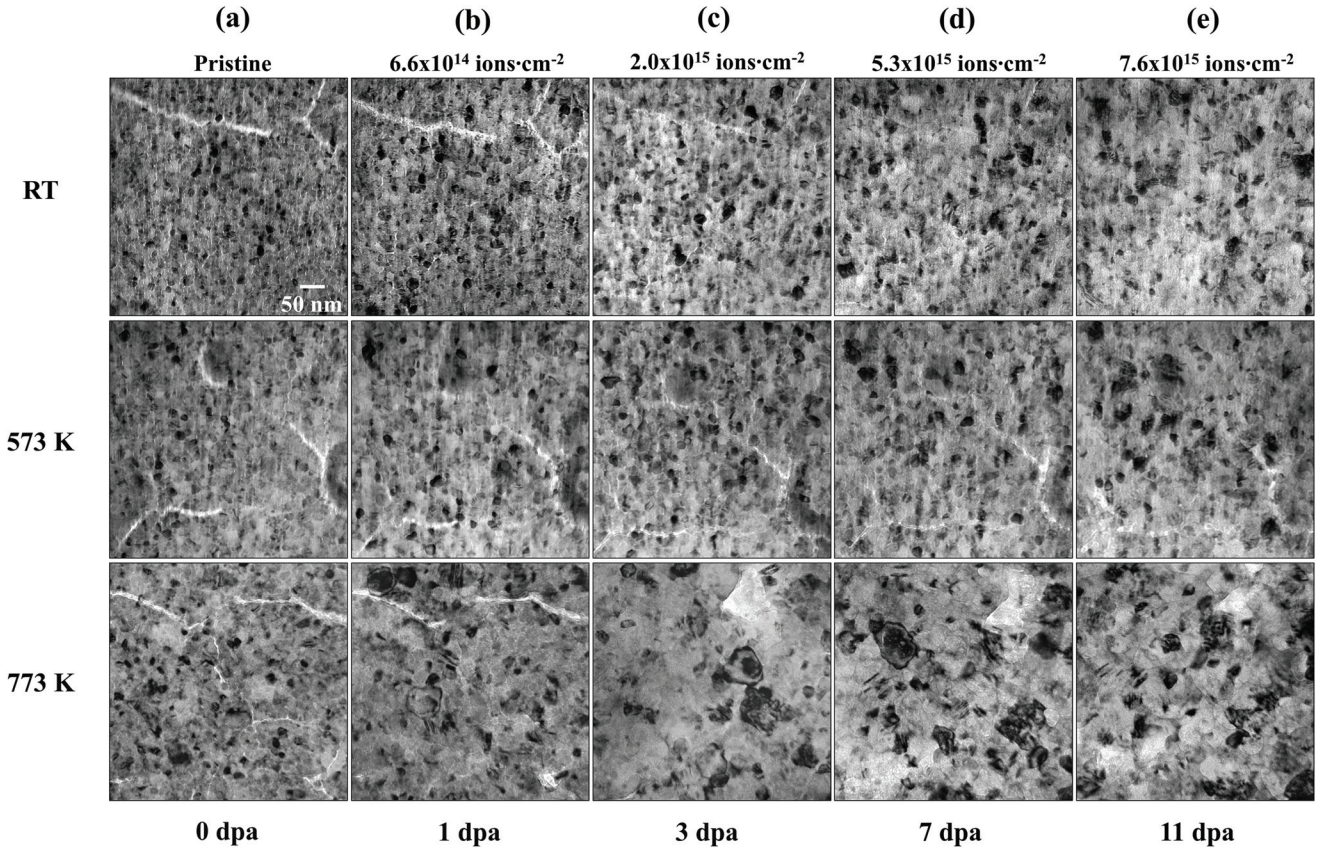

Fig. 1 Microstructural response to irradiation. Each column in the figure show BFTEM micrographs obtained during (a) thermal annealing and (b–e) the *in situ* TEM heavy ion irradiation experiments at 293, 573 and 773 K. Note: scale marker in (a) applies to all micrographs in the figure and all the images were taken using a underfocus condition of 1000 nm.

2.4. Thermal annealing *in situ* within a TEM

Thermal annealing has been carried out *in situ* within the Hitachi H-9500 TEM over 2 hours at 773 K for comparison with the microstructure of the thin films after irradiation at the same temperature. The sample after irradiation at 773 K was also annealed under the same conditions. For the *in situ* annealing experiments, the same Gatan double-tilt heating holder was used. The heating rate used in these experiments was 100 K min^{-1}. In addition, it is important to emphasize that prior to the 573 and 773 K irradiation experiments, the samples were annealed at such temperatures for 30 min in order to check for possible transformations in the microstructure solely due to annealing.

2.5. Fluence-to-dpa conversion

In order to convert fluence-to-dpa a method proposed by Stoller *et al.*[54] has been used in combination with Monte Carlo calculations within the SRIM-2013 code.[55] In this method, the "quick damage calculation mode" is used and the displacement energies for each metallic element are set to 40 eV. Under these conditions, the ion irradiation with 134 keV Xe^{+} into the CoCrCuFeNi alloy causes 898 atomic displacements per ion on average. For all the irradiated specimens, the maximum fluence was 7.6×10^{15} ions per cm^2 and given the calculated atomic density for the CoCrCuFeNi HCA (8.7×10^{22} atoms per cm^3), the maximum fluence corresponds to 11 dpa. The complete fluence-to-dpa conversion is shown in the ESI Fig. 1(c).† Although this calculation method is still in-use throughout the nuclear materials community, a recent work[56] questioned that on multi-elemental targets, the calculated dpa is often underestimated when using the quick damage calculation mode. Regardless of the fluence-to-dpa accuracy depending on SRIM's calculation modes, fluence values are given along with the estimated dpa levels for clarification.

2.6. Post-irradiation characterisation methods

The CoCrCuFeNi HCA specimens were further analysed in a FEI Talos F200X G2 S/TEM located at the Montanuniversitaet Leoben. The microscope operates a field emission gun filament at 200 keV. Super-X energy dispersive X-ray spectroscopy was used in the STEM mode aiming at elemental mapping of the pristine, irradiated and thermally annealed specimens. Differential phase contrast was also performed in the STEM mode. The size of the nanocrystalline grains during irradiation were measured within the ImageJ[57] software using a methodology already reported in the literature.[35]

3. Results

3.1. Heavy ion irradiation and annealing *in situ* within a TEM

The microstructural evolution of the nanocrystalline CoCrCuFeNi alloy under *in situ* TEM heavy ion irradiation is shown in Fig. 1. In the pristine condition, the general morphology of the synthesised material consists of nanograins (≈10 nm in diameter) within micrometer-sized sub-grains resembling voided grain boundaries: characteristic of thin solid films which grow in the zone-I of the Movchan–Demchishin–Thornton model.[58] Such voided grain boundaries are also observed around the nano-crystals in the as-deposited condition. Fig. 1, column (a) shows a series of BFTEM micrographs showing the microstructure of the alloy at 293 K and after annealing prior to irradiation at 573 and 773 K. It is worth emphasizing that the specimens were held for ≈30 min at 573 and 773 K prior to irradiation until thermal stabilisation was achieved. Still in Fig. 1, columns (b) to (e) show the microstructural evolution of the alloy within the dose range from 1 to 11 dpa at the three temperatures of interest.

The SAED patterns corresponding to the BFTEM micrographs in Fig. 1 are shown in Fig. 2 as a function of both irradiation temperature and dose. By analysing the BFTEM micrographs (Fig. 1) and SAED patterns (Fig. 2), grain growth occurred extensively at the irradiation temperature of 773 K whilst at both 293 K and 573 K, the grain growth was more modest. In the SAED patterns in Fig. 2, grain growth is noted when the polycrystalline ring-patterns start to exhibit well defined and distinct Bragg-reflection spots.

3.2. Kinetics of grain growth during irradiation

Using the BFTEM images in Fig. 1, it was possible to quantitatively estimate the microstructural evolution of the nanocrystalline alloy under annealing and irradiation by measuring the average grain size. Fig. 3 shows the average grain size as function of the irradiation dose for the three temperatures of interest. The semi-dashed lines on the plots in Fig. 3 represent non-linear fittings of the Alexander–Was model[33,59–61] for grain growth of nanocrystalline alloys under irradiation. In this model, the size of a crystal (d) under irradiation is proportional to the irradiation dose, herein represented by the fluence (Φ):

$$d^n(\Phi) = d_0^n + K\Phi \quad (1)$$

In the eqn (1), d_0 is the average grain size prior to irradiation and annealing and K is a constant related with the grain boundary mobility.[33] In the theoretical model presented

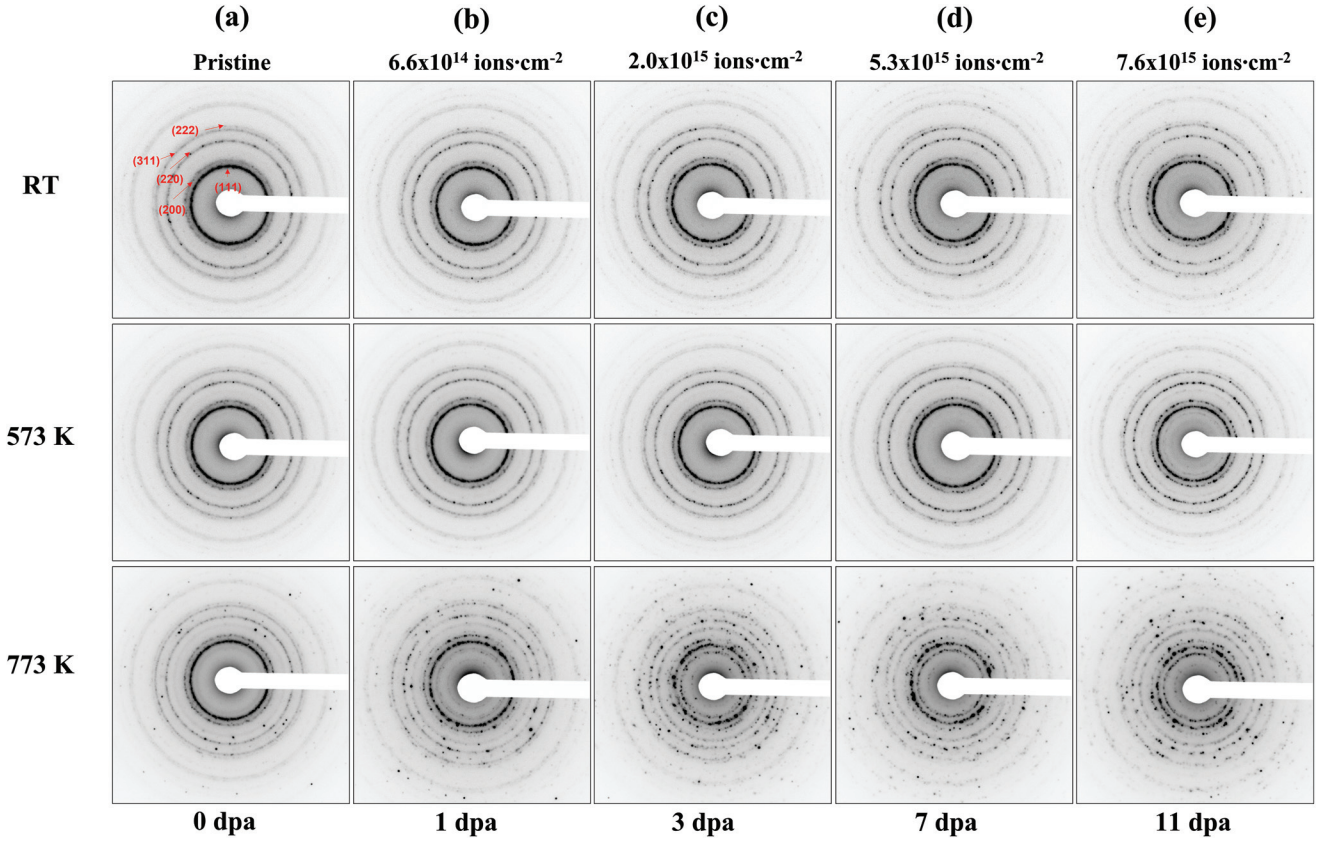

Fig. 2 Crystallographic response to irradiation. Diffraction patterns indexed with FCC structure[35] and recorded during (a) thermal annealing and (b–e) the *in situ* TEM heavy ion irradiation experiments at 293, 573 and 773 K and corresponding to the areas shown in the BFTEM micrographs in Fig. 1.

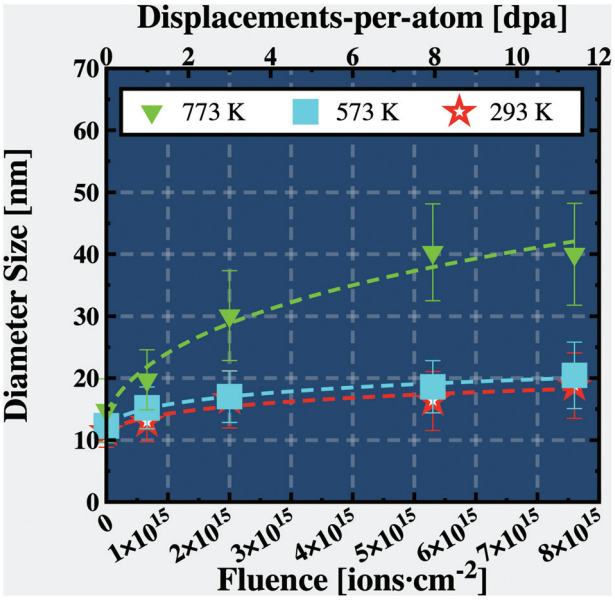

Fig. 3 Microstructural kinetics analysis. The plot shows the evolution of the nanocrystalline grain sizes as function of the irradiation dose at 293, 573 and 773 K.

in eqn (1), both K and n are fitting parameters directly dependent on the material under investigation and the annealing or irradiation temperature. The results shown in Fig. 3 follow those exhibited by Fig. 1: as the irradiation dose increases, small grain growth is observed for the irradiations at 293 and 573 K whilst the grains grew faster and larger for the irradiation at 773 K. As the samples were annealed during 30 min at both 573 and 773 K prior to irradiation, the first data points (at 0 dpa) for both blue and green curves in the Fig. 3 represent a small grain growth solely due to annealing, therefore, the grain growth herein reported is due to the effects of ion irradiation.

By fitting the average grain sizes as function of irradiation dose and temperature, it was possible to estimate the non-linear fitting parameters n and K. The results of the fittings are summarized in Table 1.

3.3. Post-irradiation and -annealing characterisation

To monitor the possible modifications in the local complex chemistry of the nanocrystalline alloy as a result of the irradiation, STEM-EDX was used to acquire high-magnification elemental maps of the CoCrCuFeNi nanocrystalline alloy before and after irradiation (final dose of 11 dpa) and after annealing. The pristine elemental composition of the nanocrystalline CoCrCuFeNi HCA as measured *via* STEM-EDX is shown in Table 2. Fig. 4 show these chemical maps for the irradiation experiments at 293 K (row a), 573 K (row b) and 773 K (row c). Two special cases were also chemically-mapped using STEM-EDX: irradiation at 773 K with subsequent annealing at 773 K after irradiation (row d) and solely annealing at 773 K (row e).

No significant modifications were observed for the irradiation experiments at both 293 K (Fig. 4 (row a)) and 573 K (Fig. 4 (row b)): the alloy has neither experienced a phase transformation nor elemental segregation as a result of irradiation. The irradiation case at 573 K exhibits segregation of Xe along the voided grain boundaries of the sub-grains, although no Xe bubbles were observed for the irradiations up to 11 dpa at both 293 and 573 K. Fig. 5(a) shows an overlay between a bright-field micrograph and Cr elemental map of the alloy irradiated up to 11 dpa at 573 K. The corresponding elemental quantification profile in Fig. 5(b) indicates enrichment of Cr along the grain boundaries of the nanocrystalline CoCrCuFeNi HCA.

On the irradiation response of the nanocrystalline CoCrCuFeNi HCA, chemical and thermodynamic phase instabilities were observed only for the irradiation at 773 K. Alterations in the local alloy chemistry at this irradiation temperature is shown in Fig. 4 (row c). As demonstrated for this irradiation case, large Xe bubbles were observed within the microstructure of the alloy (diameters between 20–60 nm as clearly exhibited in the Xe elemental map in Fig. 4 (row c). Cr segregates from the HCA single phase matrix random solid solution and it is observed to be completely segregated from the other constituents of the alloy. After irradiation at 773 K, annealing at this temperature was performed and Cr was reincorporated to the solid solution as observed in Fig. 4 (row d). Annealing after irradiation also led to the nucleation of a secondary phase rich in FeCo with a particular spherical-shape morphology. In addition, Xe bubbles were not visible after annealing the irradiated microstructure at 773 K, thus suggesting the observed Xe bubbles after irradiation may shrink and vanish (degassing) upon annealing.

In order to further investigate the formation of such FeCo secondary phase, annealing of a pristine CoCrCuFeNi HCa specimen at 773 K was performed for 2 hours *in situ* within the TEM without irradiation. The results are shown in Fig. 4 (row e): as noticeable in the elemental maps, only the anneal-

Table 1 Non-linear fitting parameters obtained from the microstructural evolution of nanocrystalline CoCrCuFeNi HCA under *in situ* TEM heavy ion irradiation

$d^n(\Phi) = d_0^n + K\Phi$	293 K	573 K	773 K
d_0 [nm]	11.4	12.3	14.3
K_m [nm^n dpa^{-1}]	1.4×10^8	1.0×10^9	1.6×10^4
n	7.3	7.7	3.2
R^2	90%	99%	97%

Table 2 Pristine elemental composition measured using STEM-EDX

Element	Atomic fraction [%]
Co	17.5 ± 2.1
Cr	17.7 ± 2.9
Cu	20.3 ± 3.4
Fe	18.7 ± 3.1
Ni	25.8 ± 4.3

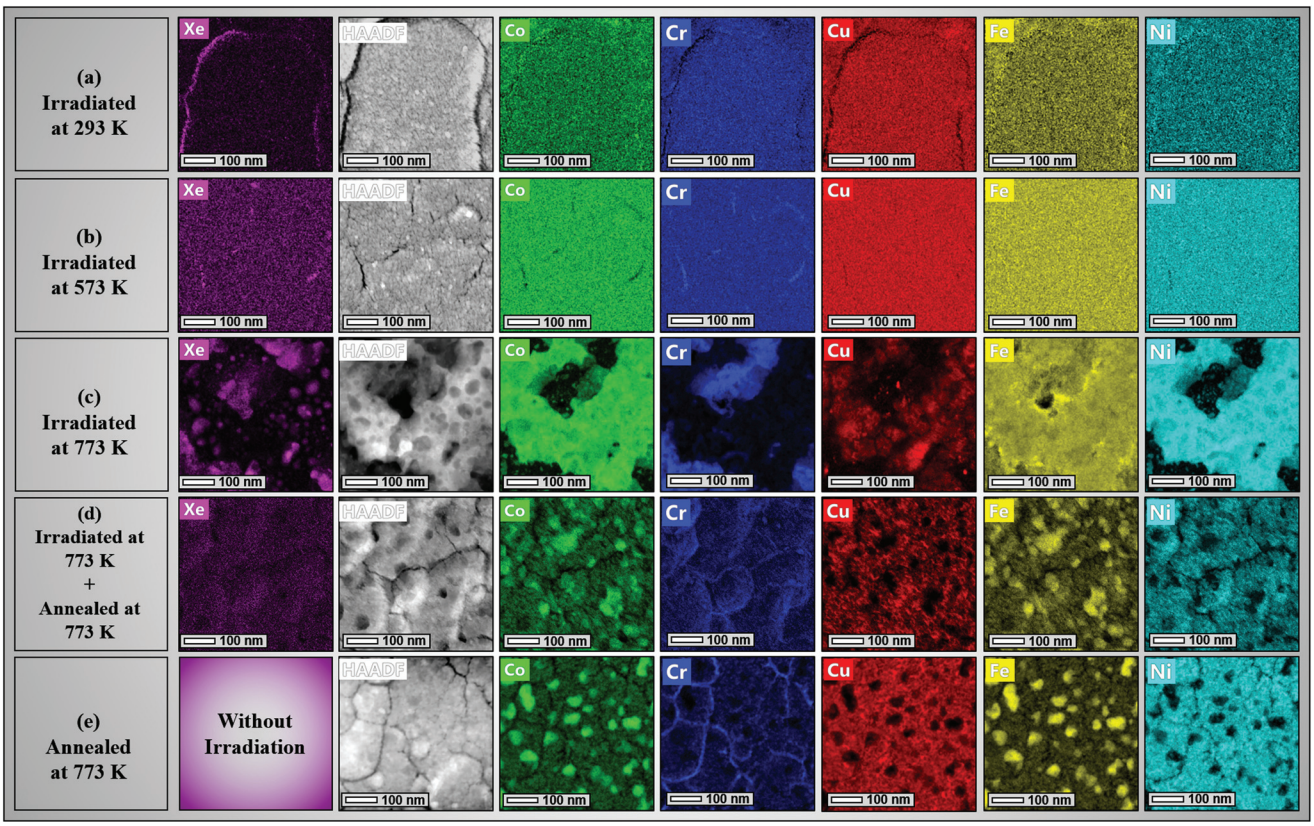

Fig. 4 Qualitative microstructural evolution of the nanocrystalline HCA. Each row in the figure has elemental maps obtained using STEM-EDX and shows the microstructural evolution of the nanocrystalline CoCrCuFeNi HCA after *in situ* TEM heavy ion irradiation up to 11 dpa at (a) 293 K, (b) 573 K and (c) 773 K. The set of STEM-EDX maps shown in the last two rows represents the microstructure of the nanocrystalline alloy after (d) annealing from its irradiated state at 773 K (c) and (e) a pristine specimen after 2 hours annealing at 773 K.

ing induces the formation of such a secondary phase. The annealing experiment also revealed strong segregation of Cr within the sub-grain boundaries.

3.4. Elemental quantification, crystallographic identification and differential phase contrast identification of FeCo magnetic nanoprecipitates

Differential phase contrast (DPC) was used to assess physical aspects of the FeCo nanoprecipitates formed after irradiation plus annealing at 773K and also solely due to annealing at 773 K (see ref. 62–70 for details on DPC microscopy and recent applications). It is worth emphasising that such FeCo nanoprecipitates also formed after annealing at 773 K from its irradiated state at 773 K (row d in Fig. 4).

The results of the DPC assessment in both pristine and annealed nanocrystalline CoCrCuFeNi HCA specimens are shown in Fig. 6. The DPC maps in Fig. 6 express the average magnetic momentum of each nanograin in the image plane (represented by the x and y components of the magnetic field, *i.e.* B_x and B_y, respectively). In the case of the pristine alloy, the components of the magnetic field are randomly oriented whilst for the annealed case, the presence of FeCo nanoprecipitates led to a strong magnetization and all the FeCo precipitates in the area have their magnetic field aligned in one preferential direction. This finding suggests that the FeCo nanoprecipitates are in fact ferromagnetic with a monodomain innerstructure.

In addition to the DPC analysis, a detailed STEM-EDX quantification of such FeCo nanoprecipitates is presented in Fig. 7(a and b). The precipitates are equiatomic in Fe and Co and highly depleted in all other initial alloying elements of the matrix phase. For such a composition as well as temperature of formation (773 K), the binary Fe–Co phase diagram indicates that this phase is the α' compound which is characterized by an ordered BCC (B2) structure.[71] Using the SAED pattern collected after annealing at 773 K, Fig. 7(e), a radial profile integration was performed to plot the reciprocal interplanar spacings as a function of the diffraction intensity. This plot is shown in Fig. 7(d) and it can be noted that low-intensity superlattice reflections corresponding to the FeCo-phase were positively detected and indexed with data available in the literature.[72,73]

4. Discussion

Two different responses based on the temperatures of both the annealing and irradiation experiments were observed: a regime in which vacancies have (presumably) low mobility (293–573 K) and another where vacancies have greater mobility

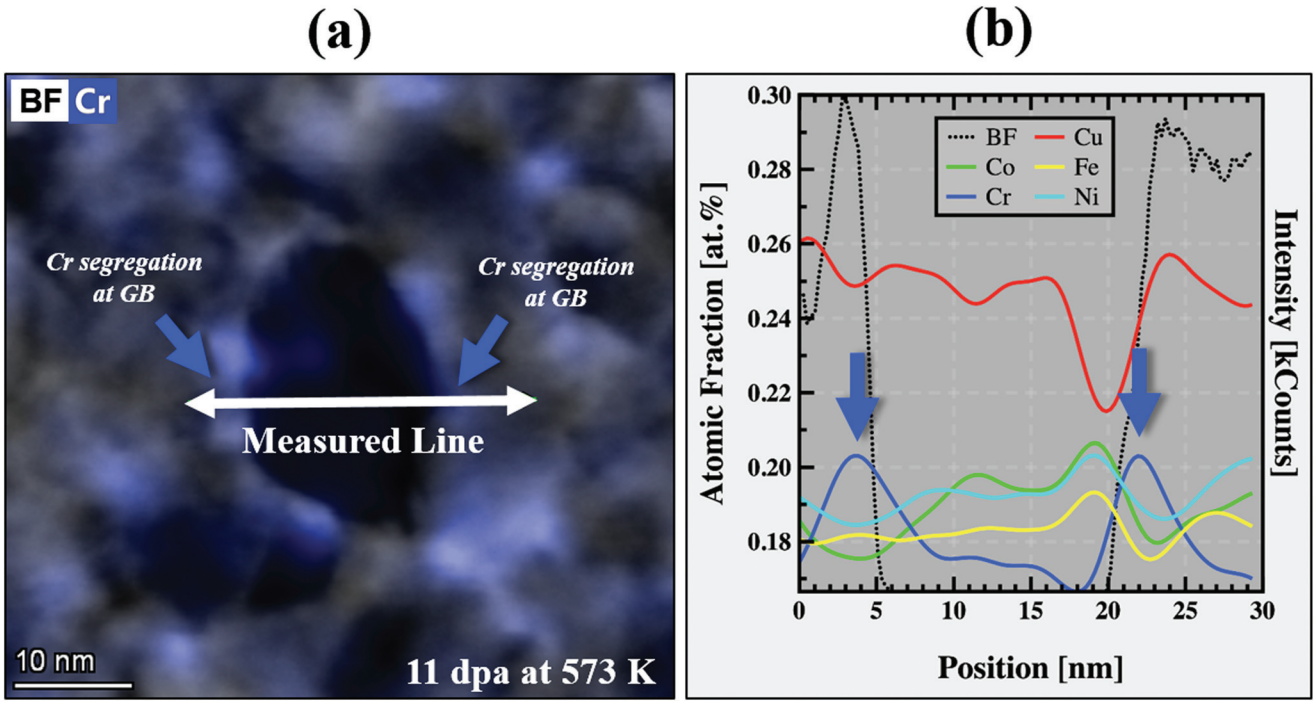

Fig. 5 Solute drag effect detected at lower irradiation temperatures (573 K). In the low temperature irradiation regime (293–573 K), the observation of Cr at the nanograin boundaries was revealed to be a key factor preventing the irradiation-induced grain growth of the nanocrystalline CoCuCrFeNi HCA. The overlay bright-field and Cr map exhibited in figure (a) confirms Cr along the nanograin boundaries as quantified by the composition profile in (b). Micrograph, STEM-EDX Cr map and subsequent quantification were acquired with a sample irradiated at 573 K up to 11 dpa. Given the errors associated with the EDX quantification, Cr is present along the nanograin boundaries only in a slightly higher concentration than the matrix. Note: the atomic fraction reported in (b) is normalised to unity.

(>773 K). The absence of chemical effects due to the more mobile interstitials suggest that the corresponding sinks are not selective for chemical species. A last major observation was the formation of the magnetic FeCo nanoprecipitates at high temperatures.

4.1. Low temperature regime (293–573 K)

The primary observation arising from the heavy ion irradiation within the range of 293–573 K is that no significant morphological alterations occurred within the microstructure of the CoCrCuFeNi HCA, thus a temperature window where the material exhibits excellent radiation resistance. Grain growth was only minor for the irradiation at 573 K after 11 dpa, and practically no growth was observed for the irradiation at 293 K. By monitoring the SAED patterns as a function of dose – rows RT and 573 K of Fig. 2 – irradiation-induced phase transformations for this temperature regime were clearly not observed to take place. With respect to the chemical mapping of the irradiated specimens up to 11 dpa in the temperature range of 293–573 K presented in Fig. 4 (rows a and b), Xe segregation along the sub-grain boundaries was observed, although no Xe bubbles were detected within the microstructures.

These results can be better evaluated with the grain growth kinetic analysis carried out with the application of the Alexander–Was model expressed by eqn (1). Kaoumi *et al.*[33] modified the original Alexander–Was model and concluded that an exponent n value around 2 corresponds to a thermally-assisted grain growth regime whereas exponent values around 3 are characteristic of irradiation-induced grain growth at low temperatures. Analysis in the grain size rate eqn (1) indicates that as a function of fluence, the final grain size value D will be dependent on n: the higher the n value, the smaller the rate of grain growth. The results obtained for nanocrystalline CoCrCuFeNi HCA under heavy ion irradiations in the temperature regime of 293–573 K indicate that the exponent n value is 7.3 and 7.7 for the temperatures of 293 and 573 K, respectively. These values are higher than those reported by Kaoumi *et al.*[33] who estimated n around 3 for heavy ion irradiation (0.5 to 1 MeV of either Ar or Kr) on nanocrystalline pure elements such as Zr, Au, Cu and Pt. This result indicates that in this lower temperature regime, grain growth under irradiation is significantly suppressed in the nanocrystalline CoCrCuFeNi HCA when compared with nanocrystalline pure metals. The same mathematical analysis discussion holds for the non-linear fitting parameter K, related with grain boundary mobility and driving force:[33] large values of K were estimated in this work for the temperature regime of 293–573 K, *i.e.* $K \approx 10^8$–10^9 whereas $K \approx 10^3$–10^5 nm^n dpa^{-1} was observed for nanocrystalline metals under irradiation according to Kaoumi *et al.*[33] This leads to the conclusion that the grain boundary mobility within the nanocrystalline CoCrCuFeNi HCA is somehow suppressed under irradiation in the mentioned temperature

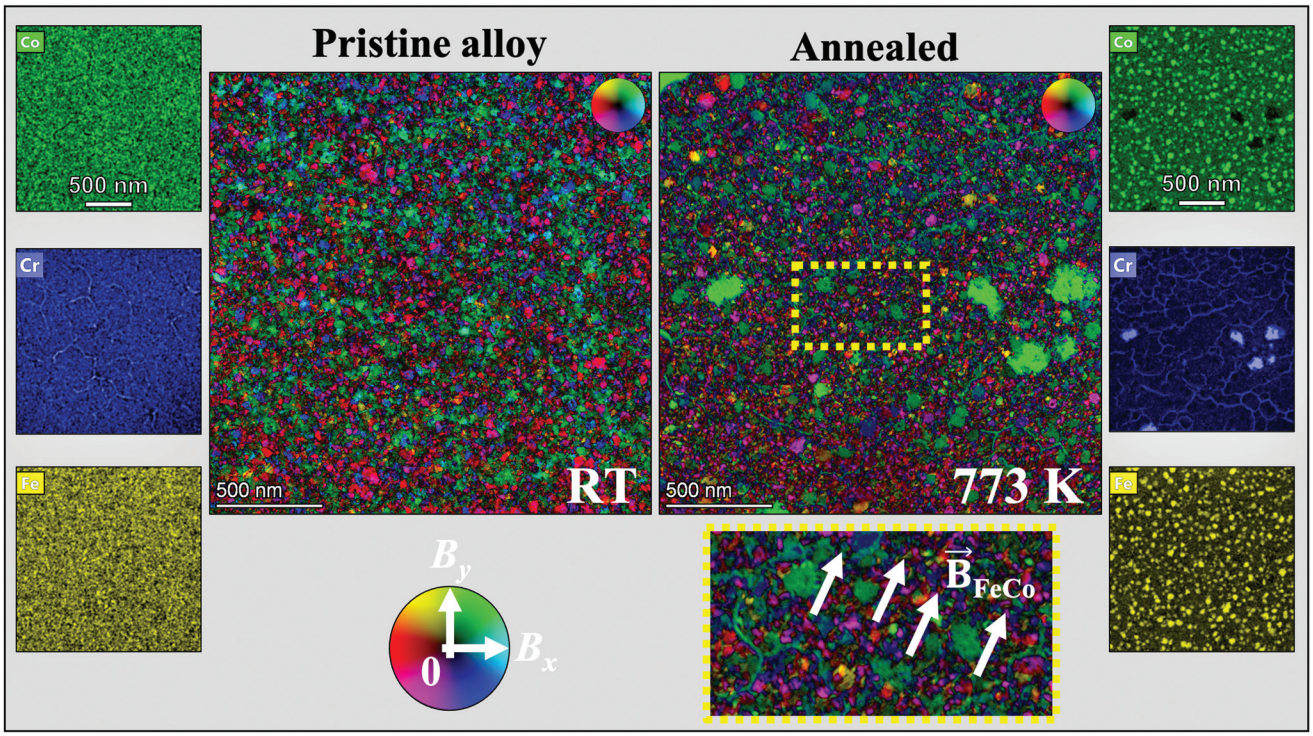

Fig. 6 Magnetic FeCo nanoprecipitates formed after annealing at 773 K. A comparison between the nanocrystalline CoCrCuFeNi HCA in its pristine form and after annealing at 773 K revealed the precipitation of FeCo magnetic nanoprecipitates out of the random solid solution matrix. Differential phase contrast (DPC) was used within the STEM to estimate the magnetic momentum of such FeCo nanoprecipitates. The DPC maps of the pristine and annealed alloy show that in the latter case ordered magnetisation for the FeCo domains is observed whilst the nanograins in the pristine and annealed case exhibit a random-like magnetisation. Note: the color wheel in the figure, represents the directions of the x and y magnetic field components estimated by the DPC.

regime. It is worth emphasizing that these values agree with recent data published by our group using *ex situ* heavy ion irradiations within the MeV energy range.[35]

A first explanation for such a suppressed grain growth under irradiation within the regime of 293–573 K is the observation of Cr along the nanograin boundaries as detected *via* STEM-EDX and shown in Fig. 5. EDX quantification of the pristine alloy as presented in Table 2 shows that the level of Cr within the matrix is around 17.7 ± 2.9 at% whereas after irradiation at 573 K, the level is 20 ± 3.0 at% at the nanograin boundaries: which is a very small difference considering the error margins of the quantification. Thus Cr is observed along the nanograin boundaries with slightly higher content than within the pristine matrix alloy, although such a difference is not large enough to unequivocally conclude there is radiation-induced segregation of Cr. In addition, such a small Cr enrichment may be caused by the 30 min of annealing solely at 573 K prior to irradiation.

Our results in this temperature regime can be understood as a particular feature of the Xe implantation, nanocrystallinity and a particular core-effect of the HCAs. The Xe atom size is relatively large when compared with the alloying elements (Xe atomic radius is 216 pm whereas the average size of the alloy constituents is ≈163 pm), thus its implantation can increase/cause the severe lattice distortion of the nanocrystalline HCA, leading to a small degree of lattice expansion due to atomic size mismatch and subsequently a small expansion of the nanograins. This allows highly mobile Cr atoms to migrate to the grain boundaries as the Cr atom size can be considered "undersized" with respect to the other alloying elements of the matrix, leading to a solute-drag effect. Such an interpretation agrees with recent literature data on ferritic/martensitic steels[74] and in the same alloy irradiated by some of the present authors with 3 MeV Ni ions up to 370 dpa.[41]

The observation of Cr at the nanograin boundaries has major implications for the exhibited high radiation tolerance of the CoCrCuNiFe nanocrystalline HCA in temperatures lower than 573 K. It is believed that such a small enrichment of Cr at intragranular positions will contribute towards mitigation of further grain growth, creating a nanocrystalline material which self-stabilizes under irradiation. The absence of further defects as well as the manifestation of phase transformations for irradiation in this temperature regime may indicate that vacancies have relatively low mobility under irradiation, therefore leading to suppressed grain growth.

4.2. High-temperature regime (>773 K)

In the temperature regime of T >573 K, matrix phase instabilities were detected in the nanocrystalline CoCrCuFeNi HCA either under heavy ion irradiation or extended annealing.

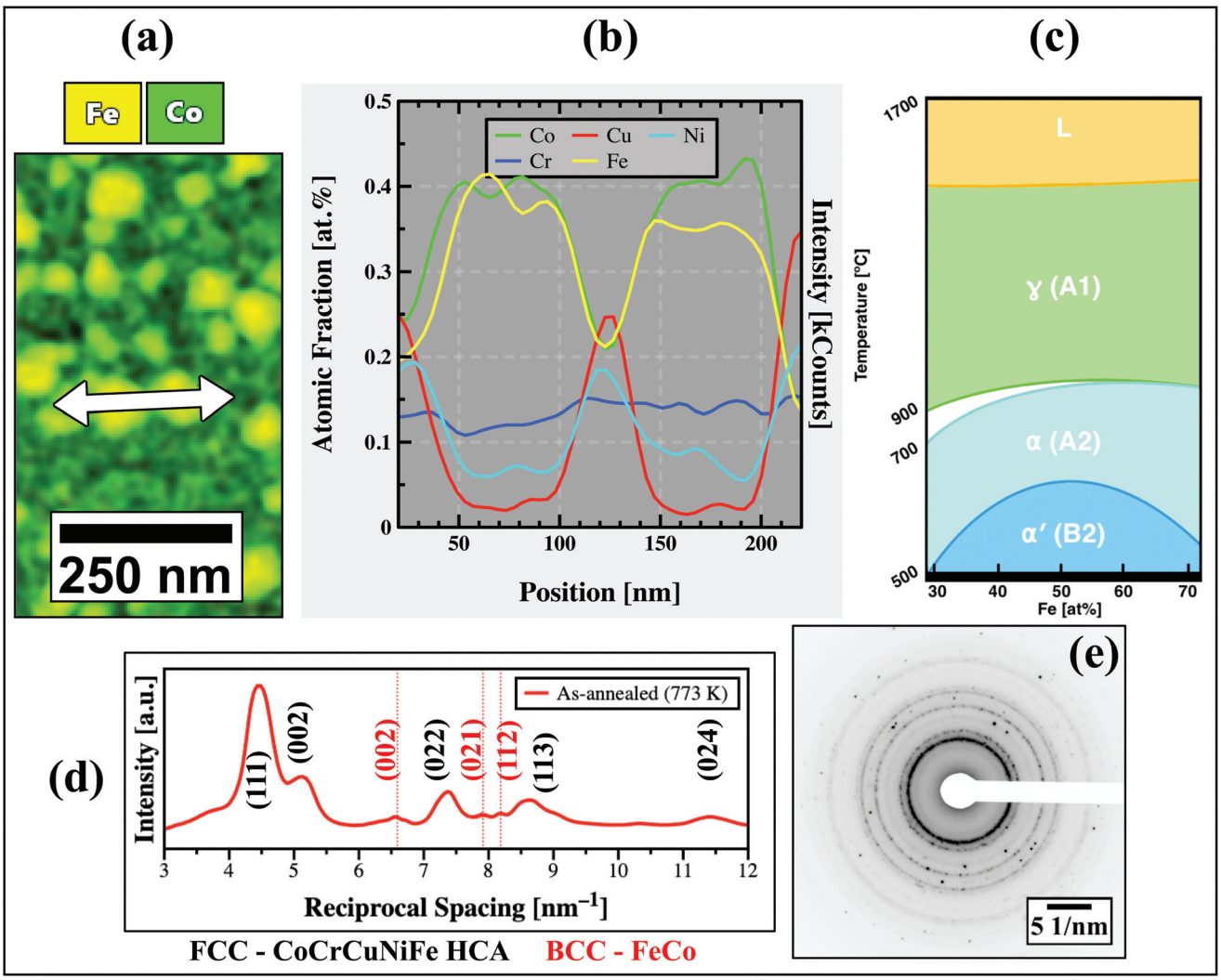

Fig. 7 FeCo elemental quantification, phase diagram and crystallographic identification. STEM-EDX quantification of the FeCo nanomagnets indicated that their stoichiometry is equiatomic as exhibited in figures (a) and (b). (c) Phase diagram analysis from data-available in literature[71] indicate this phase is the α' equilibrium phase of the binary FeCo system with a BCC (B2) crystal structure. The plot in (d) represents a radial profile integration from the SAED pattern in (e) taken after extended annealing at 773 K. Indexing of the reciprocal spacings using literature data[72,73] indicates a positive match for the FeCo-phase (extra-spots in red). Note: the atomic fraction reported in (b) is normalised to the unity.

Initially the BFTEM and SAED pattern micrographs analysis for the irradiations at 773 K as shown in the third row of Fig. 1 and 2, respectively, indicated that grain growth was pronounced at this temperature compared with the low-temperature regime.

STEM-EDX analysis presented in row (c) of Fig. 4 revealed that such grain growth is concomitant with severe Cr depletion and formation of Cr-rich zones (resembling "de-alloying") and the remaining matrix phase appears to be rich in FeCoNi with some remnants of Cu, but highly depleted in Cr. This Cr depletion from the nanograin boundaries is better visualized considering the Cu elemental map in Fig. 4 (row c) which clearly shows the nanograin boundaries. Interestingly, the Cr depletion from grain boundaries is concomitant with Cr, Fe, Co and Ni segregation (although less noticeable for Co and Ni) at the regions where a higher Xe bubbles areal density is observed, suggesting these elements tend to segregate around the Xe bubbles interfaces. It is worth emphasising that Fe, Co and Ni also segregated at the nanograin boundaries according to the elemental maps in Fig. 4 (row c).

According to He *et al.*[75] on the state-of-the-art of HCAs under irradiation, the mechanisms of RIS on these alloys are under-documented and there is a current lack of experimental results on this topic irrespective of the irradiation type (*i.e.* ions and neutrons).

In order to understand the Cr depletion and Fe, Co and Ni segregation along the nanograin boundaries in the present nanocrystalline CoCuCrFeNi HCA, we briefly overview RIS. Late in 1970s, Okamoto and Rehn defined RIS as a non-equilibrium thermodynamic process that manifest in binary and ternary alloys under irradiation at homologous temperature within the range of $0.3 \leq T_m \leq 0.5$ (where T_m is the melting point) result-

ing in the segregation or depletion of an alloy constituent at point defect sinks.[76] This segregation is dependent on the coupling of irradiation-displaced solute atoms with the influx of point defects towards sinks. Such a coupling often occurs on solutes with low self-diffusivities and the excess vacancies generated per ion collisions.[77] In this way, solutes with low diffusivities tend to segregate at interfaces whereas solutes with high diffusivities tend to deplete.

Within the nuclear materials community, this interpretation of the RIS phenomenon is known as the Inverse Kirkendall Effect (IKE).[78] IKE has been extensively used over the years to explain RIS within the microchemistry of austenitic stainless steels under irradiation.[75,79–83] These steels are cast in the ternary system Fe–Cr–Ni which is homologous to the herein studied quinary Co–Cr–Cu–Fe–Ni. In this class of steels, the element Cr has the highest diffusivity as experimentally measured by Rothman *et al.*[84] using radioactive tracers. As reported by these authors, on the ternary system Fe–Cr–Ni, the diffusivity order is $D_{Cr} < D_{Fe} < D_{Ni}$ and the reported ratios between $\frac{D_{Cr}}{D_{Ni}}$ and $\frac{D_{Fe}}{D_{Ni}}$ are 2.5 and 1.8, respectively. Under irradiation, Fe–Cr–Ni steels experience on Cr depletion and Ni enrichment at the grain boundaries. This trend of Cr depletion and Fe, Co and Ni segregation at the nanograin boundaries was observed for the heavy-ion irradiations in this present work for the nanocrystalline CoCrCuFeNi HCA, suggesting that the classical IKE effect operates in this alloy under the studied irradiation conditions.

To better understand the Cr depletion phenomenon is required, thus an extended thermal annealing experiment was performed in the irradiated alloy after the 11 dpa at 773 K irradiation. The post-irradiation and -annealing characterisation (Fig. 4 row d) showed that Cr is re-inserted into the random solid solution which apparently led to the reorganisation of the alloy's original morphology; however the formation of FeCo nanoprecipitates is noted. These FeCo precipitates are depleted of the other alloying elements, indicating that a phase transformation took place. Starting from a pristine (*i.e.* unirradiated) specimen, extended annealing at 773 K also led to the formation of such FeCo nanoprecipitates. It is also worth emphasising the intra-subgranular Cr content in the annealed specimen at 773 K (Fig. 4 row e) is visually higher than the Cr content in the irradiated plus annealed specimen at 773 K (Fig. 4 row d): while annealing only promotes Cr segregation to the subgrain boundaries, the irradiation plus annealing presents strong Cr depletion at all interfaces, thus following the IKE concepts introduced above. Comparing the annealed and irradiated to the annealed only, the morphology and general aspect of the FeCo nanoprecipitates seems to be complete in the annealed only specimen and not completed in the annealed plus irradiated specimen. This suggests the formation of FeCo nanoprecipitates is somehow favoured upon reincorporation of Cr back into the solid solution.

The observed results within this temperature regime suggest that vacancies have high mobility in this nanocrystalline HCA alloy, despite some of the constitutive core-effects of HCAs such as sluggish-diffusion of defects and high matrix phase stability for the classic Cantor's alloy when exposed to high temperatures.[8,12,85,86]

Such affirmation above is supported by two major experimental results. Firstly, Xe bubbles observed within this temperature regime were relatively large, with sizes within the range of 20–60 nm. This is of significance as in order for bubbles to grow (without coalescence), a continuous arrival of vacancies (and also Xe interstitials) is required and the final size of an equilibrium bubble is proportional by this vacancy influx until the its internal pressure is balanced with its surface energy (*i.e.* $p = \frac{2\gamma}{r}$ where p is the internal pressure, γ is the surface energy and r the bubble radius[87]). Additionally, upon annealing after irradiation at 773 K, Xe bubbles escape through the surfaces of the lamellae which takes place when the bubbles reach the lamellae surface. The second experimental observation that suggests a high mobility of vacancies in this temperature regime is the massive reorganisation of the alloy's local chemistry either under irradiation or annealing. Excess vacancies are required for Cr to segregate out of solid solution under irradiation according to the IKE model. In addition, the formation of FeCoNi- and Cr-rich partitioned zones are dependent on these excess vacancies as solid-state diffusion is required.

Within the wide range of experimental conditions studied, the microstructures of the irradiations with subsequent annealing at 773 K (Fig. 4 row d) and after annealing only (*i.e.* without irradiation) at 773 K (Fig. 4 row e) are very similar, which confirms that the irradiated alloy can be restored to its annealed state at the temperature regime where vacancies are mobile. This indicates that the alloy in its as-deposited state is found to be in a metastable condition and upon annealing at high temperatures, a new equilibrium state is achieved: the FCC CoCrCuFeNi HCA alloy plus the BCC FeCo nanoprecipitates with the observed microstructure after only irradiation at 773 K being a non-equilibrium state condition. As for better understanding of the grain growth phenomenon under irradiation, further studies are also required to evaluate the interaction between point defects, grain boundary mobility and irradiation temperature, in particular for the case of nanocrystalline HCAs such as the CoCrCuFeNi in this work.[88]

4.3. A brief comment on the radiation response of the nanocrystalline CoCrCuFeNi in the face of recent literature data

Despite the considerable level of radiation resistance observed in the temperature range from 293 to 573 K, the thermodynamic instabilities observed in the nanocrystalline CoCrCuFeNi HCA at 773 K are a limiting factor against the possible application of this alloy in the modern design of nuclear reactors operating at high-temperatures. In the face of the results observed in this work, different nanocrystalline HCAs have exhibited superior radiation resistance. The nanocrystalline WTaCrV HCA was observed to exhibit impressive radiation resistance under dual-beam *in situ* TEM ion irradiation (Kr irradiation and He implantation) at even higher irradiation temperatures than his present work: 1073 K.[28]

Similarly, a dual-phase nanocrystalline Cr_2AlC MAX phase was found to be resistant against amorphization and defect generation under 300 keV Xe implantation[89] (similar irradiation conditions to this present work).

Although the nanocrystalline HCA herein under investigation may not be suitable for application in harsh environments at high-temperatures, the data in this work indicate that not all HCA can be considered radiation resistant without a detailed study over a wide range of temperatures and large irradiation doses.

4.4. Formation of magnetic FeCo nanoprecipitates and technological implications

The thermodynamic instabilities observed to take place in the nanocrystalline CoCrCuFeNi HCA at 773 K led to a significant discovery: the formation of FeCo nanoprecipitates which were confirmed to exhibit magnetism at the nanoscale as measured with DPC technique (Fig. 6).

Achieving ferromagnetic properties in nanocrystalline materials is a recurrent challenge within the field of nanotechnology. Despite the fact bulk equiatomic FeCo magnetic alloys were firstly synthesized around 1920s,[90–92] this present work demonstrated that FeCo nanomagnets can be easily synthesized *via* thermal annealing at relatively intermediate temperatures (773 K) starting with a nanocrystalline CoCrCuFeNi HCA (as-deposited) and, more important, they remain thermodynamically stable at room temperature (which is a challenge to achieve on nanoscale magnetic materials field[93]). Another experimental observation is that the FeCo nanomagnets appear not to be stable under heavy ion irradiation, undergoing ballistic-assisted dissolution and mixing;[94,95] however, they can be restored upon annealing after irradiation which suggests they are highly stable.

FeCo nanoprecipitates were also observed by Rao *et al.*[96] to form in a FeCoNiMnCu coarse-grained HCA, but only due to thermal annealing. These authors carried out magnetization and Curie temperature measurements and indicated that this FeCo-rich nanophase has potential magnetic properties which fosters new technological applications. In addition, a comprehensive atom probe tomography (APT) study was performed by these authors to characterize the FeCo-phase over a broad range of temperatures, in agreement with the STEM-EDX characterization presented in our work. These works demonstrate that the matrix degradation of HCAs *via* phase transformations can be used to design materials with unique properties, although HCAs had been previously believed to have a high degree of stability only due to "high-entropy" stabilization of a single phase regardless of their chemical constitution.

Ordered compounds (in their bulk forms, not as nanoprecipitates) like the herein observed FeCo nanomagnets have been reported to exhibit excellent ferromagnetic properties such as high magnetic saturation, high permeability and, more importantly, high coercivity.[90] The latter is a measure of "magnetic hardness" which is the ability to retain a magnetic field after the removal of external driving forces,[93] which is inversely proportional to the grain size. This suggests that the FeCo nanomagnets are promising materials to be studied within the field of spintronics[97] as due to their reduced dimensions at the nanoscale, a competition between the quantum mechanical exchange and magnetostatic energies results in the generation of single giant spins according to Brown's theory of fine-magnetic particles.[98] Such an effect has been extensively studied in semiconductors *via* absorption of single photons which induce the generation of giant spin polarons thousands of times higher than the Bohr's magneton.[99]

The presence of FeCo nanomagnets as observed in this work could be further explored in the context of micro-nano devices, an emerging new field of research where electromagnetic fields and radiation can be manipulated in solid-state at the nanoscale.[100,101] In addition, measurements on coercivity, saturation magnetization and Curie temperature estimation should be carried out following the discoveries reported on this present work regarding the presence of FeCo nanomagnets. A present limitation to perform such magnetization measurements is the thickness of the magnetron-sputtered CoCrCuNiFe nanocrystalline HCA films (around 70 nm) and the size of the FeCo nanomagnets which may generate signals of low intensity, thus impairing the magnetic measurements using conventional magnetometer techniques. A recent paper performed nanoscale measurements on the magnetic properties of FeCo-rich nanomagnets using spin-polarized scanning tunneling microscopy (SP-STM) and their potential for applications in emerging technological areas was fully revealed.[102]

5. Conclusions

An irradiation assessment of a novel nanocrystalline CoCrCuFeNi HCA (a modified version of original Cantor's alloy CoCrMnFeNi) was performed over a wide range of temperatures and up to a dose of 11 dpa using heavy ion irradiation with *in situ* TEM with the objective of investigating the stability of this alloy at both high-temperatures and considerable irradiation doses.

A comprehensive assessment using *in situ* TEM ion irradiation and post-irradiation S/TEM analysis was performed and the obtained results allowed the identification of two different regimes of radiation responses pertaining to the mobility of irradiation-induced defects within the alloy microstructure:

- In the first regime of irradiation within the temperature range from 293 to 573 K, no significant alterations were observed to occur within the alloy's initial microstructure and a high degree of radiation tolerance was observed. Grain growth was minor due to the slight enrichment of Cr along the nanograin boundaries which is not high enough in elemental content to indicate that RIS took place. In this temperature regime, neither Xe bubbles nor phase transformations were observed to take place, thus vacancies were considered to have low mobility.
- In the second irradiation temperature range, specifically at 773 K, matrix phase instabilities were detected and characterized using electron-microscopy methods. Irradiation at 773 K led to matrix phase decomposition into a CoCuFeNi-rich phase and regions with high depletion of the element Cr

pointing to the occurrence of the classical inverse Kirkendall effect as it happens for austenitic stainless steels under irradiation (Fe–Cr–Ni). The nucleation of large Xe bubbles as well as alterations in the alloy's local chemistry led to the indication that vacancies are mobile in this regime. Annealing after irradiation at 773 K led to the formation of a CoCuCrFeNi matrix and the precipitation of nanoscale FeCo monodomains. The latter microstructure was also reproduced only *via* annealing the pristine alloy at 773 K, suggesting that the thermodynamic equilibrium state of this quinary system can be composed of FCC CoCuCrFeNi as the matrix phase along with the BCC ordered FeCo nanoprecipitates: indicating that the as-deposited alloy is metastable.

Despite the instabilities observed at intermediate temperatures which may limit the application of this nanocrystalline alloy as a structural material for nuclear reactors, we report a new way to synthesize FeCo nanoprecipitates which exhibit magnetic properties upon DPC assessment within the analytical electron-microscope. These FeCo nanomagnets were also previously characterized to possess excellent magnetic properties to be considered as candidate materials for further investigations within the scope of spintronics, as their reduced dimensions may give rise to unique magneto-transport and magnetic properties given the high-magnetic saturation, high-permeability and high-coercivity often exhibited by bulk FeCo alloys. Such FeCo nanomagnets could also be further studied within the context of the emerging field of micro-nano devices where electromagnetic fields can be manipulated at the nanoscale.

Therefore, the present research work suggests that thermodynamic instabilities in novel high-entropy alloys can actually be beneficial to technological areas where the synthesis of complex materials is a major concern. In addition, the thermodynamic instabilities detected experimentally in this work can support a subsequent in-depth thermodynamic assessment of the quinary CoCuCrFeNi alloy system.

Author contributions

M. A. T.: Conceptualization, visualization, data curation, investigation, methodology, writing – original draft. G. G.: Conceptualization, resources, visualization, data curation, investigation, methodology, writing – review & editing. P. D. R., W. L. B., C. G. S., S. A. M., Y. Z., S. P. and O. E. A.: Investigation, project administration, resources, validation, funding acquisition, conceptualization, supervision, writing – review & editing.

Conflicts of interest

The authors declare no conflict of interest.

Acknowledgements

Research presented in this article was supported by the Laboratory Directed Research and Development program of Los Alamos National Laboratory under project number 20200689PRD2. O. E. A. acknowledges support from the Laboratory Directed Research and Development program of Los Alamos National Laboratory under the early career program project number 20210626ECR. We are grateful to the European Research Council (ERC) excellent science grant "TRANSDESIGN" through the Horizon 2020 programme under contract 757961 and by the financial support from the Austrian Research Promotion Agency (FFG) in the project 3DnanoAnalytics (FFG-No 858040). P. D. R. acknowledges support from the Center for Nanophase Materials Sciences, which is a DOE Office of Science User Facility. C. G. S. acknowledges partial financial support by the São Paulo State Research Funding Agency (FAPESP, São Paulo, Brazil), under grant no. 2016/25248-3, and by the Brazilian National Research Council (CNPq, Brasília, Brazil) under the grant 312424/2013-2. All the authors are grateful to the Engineering and Physical Sciences Research Council (EPRSC) for funding the MIAMI facility under the grants EP/E017266/1 and EP/M028283/1. This work was partially supported by the Energy Dissipation to Defect Evolution (EDDE) programme, an Energy Frontier Research Center funded by the U.S. Department of Energy, Office of Science, Basic Energy Sciences under contract number DE-AC05-00OR22725. M. A. T. would like to thank T.M. Kremmer (MUL) for useful discussions on electron-microscopy and for his training on the Thermo Fisher Talos F200X, Prof. A.B. Henriques (USP) for discussions on Atomic and Molecular Physics and Prof. S.E. Donnelly (HUD) with assistance in sample preparation.

References

1 B. Cantor, I. Chang, P. Knight and A. Vincent, *Mater. Sci. Eng., A*, 2004, **375**, 213–218.
2 B. Cantor, *Prog. Mater. Sci.*, 2020, 100754.
3 G. Qin, R. Chen, P. K. Liaw, Y. Gao, L. Wang, Y. Su, H. Ding, J. Guo and X. Li, *Nanoscale*, 2020, **12**, 3965–3976.
4 D. B. Miracle, *JOM*, 2017, **69**, 2130–2136.
5 D. B. Miracle and O. N. Senkov, *Acta Mater.*, 2017, **122**, 448–511.
6 M. C. Gao, J. W. Yeh, P. K. Liaw and Y. Zhang, *High-entropy alloys*, Springer International Publishing, Cham, 2016.
7 M. A. Tunes, H. Le, G. Greaves, C. G. Schön, H. Bei, Y. Zhang, P. D. Edmondson and S. E. Donnelly, *Intermetallics*, 2019, **110**, 106461.
8 C. G. Schön, M. A. Tunes, R. Arróyave and J. Ågren, *CALPHAD: Comput. Coupling Phase Diagrams Thermochem.*, 2020, **68**, 101713.
9 M. Tunes, G. Greaves, H. Bei, P. Edmondson, Y. Zhang, S. Donnelly and C. Schön, *Intermetallics*, 2021, **132**, 107130.
10 J. Dabrowa, M. Zajusz, W. Kucza, G. Cieślak, K. Berent, T. Czeppe, T. Kulik and M. Danielewski, *J. Alloys Compd.*, 2019, **783**, 193–207.

11 H. K. D. H. Bhadeshia, *Mater. Sci. Technol.*, 2015, **31**(10), 1139–1141.
12 S. V. Divinski, A. V. Pokoev, N. Esakkiraja and A. Paul, *A mystery of "sluggish diffusion" in high-entropy alloys: the truth or a myth?*, Trans Tech Publications Ltd., 2018, vol. 17, pp. 69–104.
13 A. Paul, *Scr. Mater.*, 2017, **135**, 153–157.
14 Y. Li, D. Raabe, M. Herbig, P. P. Choi, S. Goto, A. Kostka, H. Yarita, C. Borchers and R. Kirchheim, *Phys. Rev. Lett.*, 2014, **113**, 1–5.
15 Y. Lu, X. Gao, Y. Dong, T. Wang, H. L. Chen, H. Mao, Y. Zhao, H. Jiang, Z. Cao, T. Li and S. Guo, *Nanoscale*, 2018, **10**, 1912–1919.
16 H. Gleiter, *Acta Mater.*, 2000, **48**, 1–29.
17 H. Van Swygenhoven, P. Derlet and A. Frøseth, *Acta Mater.*, 2006, **54**, 1975–1983.
18 K. Lu and N. Hansen, *Scr. Mater.*, 2009, **60**, 1033–1038.
19 X. Feng, J. Zhang, K. Wu, X. Liang, G. Liu and J. Sun, *Nanoscale*, 2018, **10**, 13329–13334.
20 Y. F. Zhao, J. Y. Zhang, Y. Q. Wang, K. Wu, G. Liu and J. Sun, *Nanoscale*, 2019, **11**, 11340–11350.
21 Y. F. Zhao, X. B. Feng, J. Y. Zhang, Y. Lu, S. H. Wu, Y. Q. Wang, K. Wu, G. Liu and J. Sun, *Nanoscale*, 2020, **12**, 14135–14149.
22 Y. Xie, T. Xia, D. Zhou, Y. Luo, W. Zeng, Z. Zhang, J. Wang, J. Liang and D. Zhang, *Nanoscale*, 2020, **12**, 5347–5352.
23 M. Rose, A. Balogh and H. Hahn, *Nucl. Instrum. Methods Phys. Res., Sect. B*, 1997, **127**, 119–122.
24 A. Kilmametov, D. Gunderov, R. Valiev, A. Balogh and H. Hahn, *Scr. Mater.*, 2008, **59**, 1027–1030.
25 E. Aydogan, E. Martinez, K. March, O. El-Atwani, D. Krumwiede, P. Hosemann, T. Saleh and S. A. Maloy, *Sci. Rep.*, 2019, **9**, 8345.
26 O. El-Atwani, J. Gigax, M. Chancey, J. Baldwin and S. Maloy, *Scr. Mater.*, 2019, **166**, 159–163.
27 O. El-Atwani, E. Esquivel, E. Aydogan, E. Martinez, J. Baldwin, M. Li, B. P. Uberuaga and S. A. Maloy, *Acta Mater.*, 2019, **165**, 118–128.
28 O. El-Atwani, N. Li, M. Li, A. Devaraj, J. Baldwin, M. Schneider, D. Sobieraj, J. Wróbel, D. Nguyen-Manh, S. A. Maloy, *et al.*, *Sci. Adv.*, 2019, **5**, eaav2002.
29 T. Nagase, P. D. Rack, J. H. Noh and T. Egami, *Intermetallics*, 2015, **59**, 32–42.
30 Y. Zhang, D. S. Aidhy, T. Varga, S. Moll, P. D. Edmondson, F. Namavar, K. Jin, C. N. Ostrouchov and W. J. Weber, *Phys. Chem. Chem. Phys.*, 2014, **16**, 8051–8059.
31 Y. Zhang, P. D. Edmondson, T. Varga, S. Moll, F. Namavar, C. Lan and W. J. Weber, *Phys. Chem. Chem. Phys.*, 2011, **13**, 11946–11950.
32 W. Voegeli, K. Albe and H. Hahn, *Nucl. Instrum. Methods Phys. Res., Sect. B*, 2003, **202**, 230–235.
33 D. Kaoumi, A. T. Motta and R. C. Birtcher, *J. Appl. Phys.*, 2008, **104**(7), 073525.
34 O. El-Atwani, J. A. Hinks, G. Greaves, J. P. Allain and S. A. Maloy, *Mater. Res. Lett.*, 2017, **5**, 343–349.
35 Y. Zhang, M. A. Tunes, M. L. Crespillo, F. Zhang, W. L. Boldman, P. D. Rack, L. Jiang, C. Xu, G. Greaves, S. E. Donnelly, L. Wang and W. J. Weber, *Nanotechnology*, 2019, **30**, 294004.
36 C. M. Barr, S. M. Foiles, M. Alkayyali, Y. Mahmood, P. M. Price, D. P. Adams, B. L. Boyce, F. Abdeljawad and K. Hattar, *Nanoscale*, 2021, **13**(6), 3552–3563.
37 A. Meldrum, L. Boatner and R. Ewing, *Phys. Rev. Lett.*, 2001, **88**, 025503.
38 T. Waitz, V. Kazykhanov and H. Karnthaler, *Acta Mater.*, 2004, **52**, 137–147.
39 Y. Zhang, W. Jiang, C. Wang, F. Namavar, P. D. Edmondson, Z. Zhu, F. Gao, J. Lian and W. J. Weber, *Phys. Rev. B: Condens. Matter Mater. Phys.*, 2010, **82**, 184105.
40 V. J. Angadi, A. Anupama, H. K. Choudhary, R. Kumar, H. Somashekarappa, M. Mallappa, B. Rudraswamy and B. Sahoo, *J. Solid State Chem.*, 2017, **246**, 119–124.
41 L. Jiang, Y.-J. Hu, K. Sun, P. Xiu, M. Song, Y. Zhang, W. L. Boldman, M. L. Crespillo, P. D. Rack, L. Qi, *et al.*, *Adv. Mater.*, 2020, **32**, 2002652.
42 P. K. Suri, J. E. Nathaniel, N. Li, J. K. Baldwin, Y. Wang, K. Hattar and M. L. Taheri, *Sci. Rep.*, 2020, **10**, 1–10.
43 Y. Zhang, T. T. Zuo, Z. Tang, M. C. Gao, K. A. Dahmen, P. K. Liaw and Z. P. Lu, *Prog. Mater. Sci.*, 2014, **61**, 1–93.
44 F. Granberg, K. Nordlund, M. W. Ullah, K. Jin, C. Lu, H. Bei, L. Wang, F. Djurabekova, W. Weber and Y. Zhang, *Phys. Rev. Lett.*, 2016, **116**, 135504.
45 L. Koch, F. Granberg, T. Brink, D. Utt, K. Albe, F. Djurabekova and K. Nordlund, *J. Appl. Phys.*, 2017, **122**, 105106.
46 C. Lu, L. Niu, N. Chen, K. Jin, T. Yang, P. Xiu, Y. Zhang, F. Gao, H. Bei, S. Shi, *et al.*, *Nat. Commun.*, 2016, **7**, 1–8.
47 T. Yang, S. Xia, S. Liu, C. Wang, S. Liu, Y. Fang, Y. Zhang, J. Xue, S. Yan and Y. Wang, *Sci. Rep.*, 2016, **6**, 1–8.
48 S. Zhao, Y. Osetsky and Y. Zhang, *Acta Mater.*, 2017, **128**, 391–399.
49 S. Zhao, W. J. Weber and Y. Zhang, *JOM*, 2017, **69**, 2084–2091.
50 L. J. Santodonato, Y. Zhang, M. Feygenson, C. M. Parish, M. C. Gao, R. J. Weber, J. C. Neuefeind, Z. Tang and P. K. Liaw, *Nat. Commun.*, 2015, **6**(1), 1–13.
51 X. D. Xu, P. Liu, S. Guo, A. Hirata, T. Fujita, T. G. Nieh, C. T. Liu and M. W. Chen, *Acta Mater.*, 2015, **84**, 145–152.
52 Z. An, H. Jia, Y. Wu, P. D. Rack, A. D. Patchen, Y. Liu, Y. Ren, N. Li and P. K. Liaw, *Mater. Res. Lett.*, 2015, **3**, 203–209.
53 G. Greaves, A. Mir, R. Harrison, M. Tunes, S. Donnelly and J. Hinks, *Nucl. Instrum. Methods Phys. Res., Sect. At*, 2019, **931**, 37–43.
54 R. E. Stoller, M. B. Toloczko, G. S. Was, A. G. Certain, S. Dwaraknath and F. A. Garner, *Nucl. Instrum. Methods Phys. Res., Sect. B*, 2013, **310**, 75–80.
55 J. F. Ziegler, M. D. Ziegler and J. P. Biersack, *Nucl. Instrum. Methods Phys. Res., Sect. B*, 2010, **268**, 1818–1823.
56 W. J. Weber and Y. Zhang, *Curr. Opin. Solid State Mater. Sci.*, 2019, **23**, 100757.

57 C. A. Schneider, W. S. Rasband and K. W. Eliceiri, *Nat. Methods*, 2012, **9**, 671–675.
58 J. A. Thornton, *J. Vac. Sci. Technol., A*, 1986, **4**, 3059–3065.
59 D. E. Alexander, G. S. Was and L. Rehn, *J. Appl. Phys.*, 1991, **70**, 1252–1260.
60 D. E. Alexander, G. S. Was and L. Rehn, *Nucl. Instrum. Methods Phys. Res., Sect. B*, 1991, **59**, 462–466.
61 D. E. Alexander and G. S. Was, *Phys. Rev. B: Condens. Matter Mater. Phys.*, 1993, **47**, 2983.
62 K. Tsuno, M. Inoue and K. Ueno, *J. Mater. Sci. Eng. B*, 1989, **3**, 403–407.
63 M. R. McCartney, P. Kruit, A. H. Buist and M. R. Scheinfein, *Ultramicroscopy*, 1996, **65**, 179–186.
64 N. Shibata, S. D. Findlay, Y. Kohno, H. Sawada, Y. Kondo and Y. Ikuhara, *Nat. Phys.*, 2012, **8**, 611–615.
65 J. Zweck, *J. Phys.: Condens. Matter*, 2016, **28**(40), 403001.
66 N. Shibata, S. D. Findlay, T. Matsumoto, Y. Kohno, T. Seki, G. Sánchez-Santolino and Y. Ikuhara, *Acc. Chem. Res.*, 2017, **50**, 1502–1512.
67 G. Lee, J. Jeong, F. Schwarzhuber, J. Zweck, J. Kim, D. H. Kim and H. J. Chang, *Micron*, 2019, **127**, 102755.
68 L. Angeloni, D. Passeri, S. Corsetti, D. Peddis, D. Mantovani and M. Rossi, *Nanoscale*, 2017, **9**, 18000–18011.
69 D. Avram, C. Colbea, M. Florea, S. Lazar, D. Stroppa and C. Tiseanu, *Nanoscale*, 2019, **11**, 16743–16754.
70 M. Campanini, E. Gradauskaite, M. Trassin, D. Yi, P. Yu, R. Ramesh, R. Erni and M. D. Rossell, *Nanoscale*, 2020, **12**, 9186–9193.
71 T. Nishizawa and K. Ishida, *Bull. Alloy Phase Diagrams*, 1984, **5**, 250.
72 J. W. Edington and K. T. Russell, *Practical electron microscopy in materials science*, Macmillan International Higher Education, 1977.
73 P. Bayliss, *Can. Mineral.*, 1990, **28**, 751–755.
74 Z. Lu, R. G. Faulkner, G. Was and B. D. Wirth, *Scr. Mater.*, 2008, **58**, 878–881.
75 M.-R. He, S. Wang, S. Shi, K. Jin, H. Bei, K. Yasuda, S. Matsumura, K. Higashida and I. M. Robertson, *Acta Mater.*, 2017, **126**, 182–193.
76 P. Okamoto and L. Rehn, *J. Nucl. Mater.*, 1979, **83**, 2–23.
77 W. Kesternich and A. Garcia-Borquez, *Scr. Mater.*, 1997, **36**, 1127–1132.
78 A. D. Marwick, *J. Phys. F: Met. Phys.*, 1978, **8**, 1849–1861.
79 S. Watanabe and H. Takahashi, *J. Nucl. Mater.*, 1994, **208**, 191–194.
80 T. R. Allen, J. T. Busby, G. S. Was and E. A. Kenik, *J. Nucl. Mater.*, 1998, **255**, 44–58.
81 T. Allen and G. Was, *Acta Mater.*, 1998, **46**, 3679–3691.
82 Y. Yang, K. G. Field, T. R. Allen and J. T. Busby, *J. Nucl. Mater.*, 2016, **473**, 35–53.
83 B. Kombaiah, P. D. Edmondson, Y. Wang, L. A. Boatner and Y. Zhang, *J. Nucl. Mater.*, 2019, **514**, 139–147.
84 S. Rothman, L. Nowicki and G. Murch, *J. Phys. F: Met. Phys.*, 1980, **10**, 383.
85 K.-Y. Tsai, M.-H. Tsai and J.-W. Yeh, *Acta Mater.*, 2013, **61**, 4887–4897.
86 K.-Y. Tsai, M.-H. Tsai and J.-W. Yeh, *Scr. Mater.*, 2017, **135**, 158–159.
87 R. Barnes, *J. Nucl. Mater.*, 1964, **11**, 135–148.
88 B. P. Uberuaga, L. J. Vernon, E. Martinez and A. F. Voter, *Sci. Rep.*, 2015, **5**, 1–9.
89 M. A. Tunes, M. Imtyazuddin, C. Kainz, S. Pogatscher and V. M. Vishnyakov, *Sci. Adv.*, 2021, **7**, eabf6771.
90 T. Sourmail, *Prog. Mater. Sci.*, 2005, **50**, 816–880.
91 Q. He, Y.-H. Chu, J. Heron, S. Yang, W. Liang, C. Kuo, H. Lin, P. Yu, C. Liang, R. Zeches, *et al.*, *Nat. Commun.*, 2011, **2**, 1–5.
92 S. Sugimoto, *Magnetic Material for Motor Drive Systems*, Springer, 2019, pp. 261–277.
93 M. E. McHenry, M. A. Willard and D. E. Laughlin, *Prog. Mater. Sci.*, 1999, **44**, 291–433.
94 G. Greaves, J. Hinks, P. Busby, N. Mellors, A. Ilinov, A. Kuronen, K. Nordlund and S. Donnelly, *Phys. Rev. Lett.*, 2013, **111**, 065504.
95 C. Sun, M. Kirk, M. Li, K. Hattar, Y. Wang, O. Anderoglu, J. Valdez, B. P. Uberuaga, R. Dickerson and S. A. Maloy, *Acta Mater.*, 2015, **95**, 357–365.
96 Z. Rao, B. Dutta, F. Körmann, W. Lu, X. Zhou, C. Liu, A. K. da Silva, U. Wiedwald, M. Spasova, M. Farle, D. Ponge, B. Gault, J. Neugebauer, D. Raabe and Z. Li, *Adv. Funct. Mater.*, 2021, **31**, 2007668.
97 A. Henriques, X. Gratens, P. Usachev, V. Chitta and G. Springholz, *Phys. Rev. Lett.*, 2018, **120**, 217203.
98 W. F. Brown Jr., *J. Appl. Phys.*, 1968, **39**, 993–994.
99 S. van Kooten, X. Gratens and A. Henriques, *Phys. Rev. B*, 2021, **103**, 035202.
100 M.-S. Cao, X.-X. Wang, M. Zhang, W.-Q. Cao, X.-Y. Fang and J. Yuan, *Adv. Mater.*, 2020, **32**, 1907156.
101 M. Zhang, C. Han, W.-Q. Cao, M.-S. Cao, H.-J. Yang and J. Yuan, *Nano-Micro Lett.*, 2021, **13**, 1–12.
102 H.-H. Yang, *Nanoscale*, 2021, DOI: 10.1039/D1NR04862G.